Creep characterisation of Inconel 718 lattice metamaterials manufactured by laser powder bed fusion

A.S. Bhuwal[a], Y. Pang[a,c], I. Maskery[b], I. Ashcroft[b], W. Sun[a], T. Liu[a,c,*]

[a]Faculty of Engineering, University of Nottingham, University Park, Nottingham NG7 2RD, UK
[b]Centre for Additive Manufacturing, Faculty of Engineering, University of Nottingham, Nottingham, Nottinghamshire NG7 2RD, UK
[c]School of Engineering and Materials Science, Queen Mary University of London, Mile End Road, London, E1 4NS, UK

*Corresponding Author: Tao.Liu@qmul.ac.uk

Abstract

Lattice metamaterials manufactured by laser powder bed fusion (LPBF) are limited by their performance for critical applications. The LPBF materials have microstructural or macroscale anomalies, such as suboptimal grain size, morphology, and lack of fusion. This results in LPBF metamaterials performance degradation for various mechanical properties, such as creep, which has seldom been researched. To understand the creep behaviour of LPBF Inconel 718, Body Centred Cubic (BCC) metamaterials were fabricated for creep test at 650 °C. Kachanov's damage modelling has been used to predict the creep performance of the metamaterials under different loading conditions. Microstructural characterisation has been performed with Scanning Electron Microscopy (SEM) to identify critical microstructure defects affecting the failure mechanisms and creep behaviour s of the metamaterials. The results show that the loading conditions affect the fracture process of the metamaterials owing to different failure mechanisms. The simulation and test results show that the logarithmic decline in creep life when loading increases; also, logarithmic increase in the creep life when relative density increases.

Keywords: *Additive manufacturing; Inconel 718; Microstructure; Lattice metamaterials; Creep;*

1. Introduction

For the last few decades, interest in manufacturing periodic or lattice metamaterials has continuously increased due to highly customised properties. In conjunction with lightweight properties, lattice structures provide impact resistance, non-conducting heat properties and electromagnetic wave absorption [1–9]. The study of lattice structure studies has continuously increased over the past decades. As a result, many researchers are

designing complex structures using lattices with different unit cells and relative densities (ratio of the density of the lattice material to the density of the solid material from which it is made). For example, Tancogne-Dejean & Mohr [10] Studied a specific design which was an isotropic elastic structure with the combination of Simple Cubic (SC), Body Centred Cubic (BCC) and Face Centred Cubic (FCC) lattices. Through periodic homogenization, it was observed that isotropic truss lattices demonstrate lower initial yield anisotropy than the octet truss lattices. They developed a few cubic trusses lattice structures similar to the grid type, which were elastically isotropic. The study illustrated that the mechanical characteristics of grid-type of truss lattice structures change as per the direction of loading. Bonatti & Mohr [11] Performed finite element (FE) analysis and compression tests on stainless steel material specimens manufactured by additive manufacturing (AM) and also examined statically-determinate solid octet truss lattice under large strain compression of different metamaterial architectures. It was observed that hollow rhombic dodecahedral mesostructures provide nearly twice the strength and energy absorption of the octet truss. The smooth changes were due to structures becoming bending-dominated to stretching-dominant.

Before advancing AM, other orthodox manufacturing technologies like investment casting, deformation forming, brazing etc., are studied to produce periodic lattice geometries. Limitations of such techniques include the fitness of the structures and the actual cell geometry [12]. Over the years, AM technologies have been developed to produce three-dimensional objects directly from a digital model by adding materials without specialised tooling. For example, laser powder bed fusion (LPBF) or Selective laser melting (SLM) can produce fine surface geometries like roughness value at 50 microns lattice structures using AM process for metal alloys. LPBF creates components layer by layer by melting specific parts of a powder bed based on a 3D CAD model with a laser beam [13]. Sing et al. (2018) [14] used LPBF to manufacture complex cellular lattice structures and determined the factors most affecting their dimensional and mechanical properties. They found that the horizontal dimensions are primarily impacted by layer thickness, and vertical and diagonal dimensions are influenced mainly by laser power. The process offers benefits for producing complex components, especially in aerospace using superalloys, as it does not require tooling and directly uses CAD data [15]. The Inconel 718 alloy is widely used in modern aircraft engines due to its high strength and elevated temperature resistance [16]. The material properties of Inconel 718, such as precipitation and solid solution hardening, allow it to maintain strength and fatigue resistance at high temperatures up to 650°C [17]. However, its desired mechanical properties make it difficult to machine, requiring special tools and specific machining parameters [18].

In contrast, the LPBF process eliminates the issue of machinability, resulting in microstructures typically composed of columnar dendrites growing along the building direction [19]. In recent years, the research on the LPBF manufacturing process of superalloy Inconel 718 has been of great interest. For example, Amato et al. (2012) [20] investigated the LPBF of Inconel 718 and examined the microstructure of the material and basic mechanical properties, such as hardness and tensile strength. They found that corresponding tensile properties LPBF of Inconel 718 were comparable with wrought Inconel 718 alloy. Furthermore, because of the unique quality of the LPBF manufacturing process that allows for tailored mechanical, thermal and biological

properties in the diffusion of lattices, trusses, and periodic materials could be found [21,22]. For microstructural study of LPBF manufacturing process, Hu et al. [23] investigated the influence of manufacturing porosity and lack of fusion defects on the fatigue resistance of SLM processed Ti-6Al-4V. They have used X-ray tomography, an accurate characterization of the defects to reveal the defect-induced failure behavior via fatigue testing. Also, Peng et al. [24] used a machine learning (ML) algorithm to correlate the observed fatigue life of laser powder bed fusion (LPBF) processed AlSi10Mg alloy to parameters characterizing the critical microstructural defects.

Although much research is going on how the high-temperature performance of LPBF components, such as their microstructures and mechanical properties, compares to those made through traditional methods [25], the high-temperature creep performance of LPBF-made Inconel 718 metamaterials has yet to be explored thoroughly. Creep is the primary failure mode at elevated temperatures, and a comprehensive creep design method is highly desirable to develop [26]. Andrews et al. [27] established expressions for the creep-bending of cell walls allowing the creep rate of honeycombs and foams to be predicted from the cell-wall properties and relative density. Fan et al. [28] investigated the uniaxial and multiaxial creep behaviour of low-density open-cell foams and proposed a modified analytical expression by considering the mass at the strut node. Su, et al. [29] established an analytical model to predict the creep strain rate of imperfect honeycombs. It was observed in the study that the creep strain rate depends on the defects density as well as the type of missing struts of imperfect honeycombs. Monkman & Grant [30] proposed an empirical relationship between the minimum creep rate and rupture life at elevated temperatures by analysing the steady-state creep rate. However, the creep performance of the metamaterials due to microstructure defects owing to the LPBF manufacturing process is still an issue.

As part of a more in-depth study, this paper aims to investigate the creep characteristics of LPBF-manufactured Inconel 718 metamaterials. The creep behaviour and effects of LPBF-made Inconel 718 metamaterials microstructural defects have been assessed. In this work, we have accurately captured the microstructure defects using Kachanov's creep damage model. The Kachanov's model considers the continuous degradation of material during creep by using a ratio of an intact area over the original area to predict creep failure times. This model type can be beneficial in modelling creep where microvoid initiation and coalescence occur. The Kachanov's model can also be even more applicable to LPBF materials with higher porosities than their conventionally manufactured equivalents. In addition, the paper examines the leading causes of specimen failure and the effects of loading and relative density on creep life.

The paper is organised as follow. The details of parent material i.e., Inconel 718 and manufacturing process of metamaterials are presented in Section 2 along with experimental study and numerical modelling. The mechanical behaviours such as tensile and creep characteristics of the metamaterials at high temperature are described in Section 3. The results of the numerical simulations are presented and discussed in detail in Section 4 along with microstructure study of the manufacturing process. Section 5 contains concluding remarks and suggestions for further research.

2. Material and experimental testing

2.1. Material and manufacturing

In this work, all specimens were built using a Renishaw© and commercially available Inconel 718 alloy powder. The chemical composition of the Inconel 718, to manufacture metamaterial produced by LBPF investigated in this study given in Table 1 [31]. The powder particles constituted a spherical shape and an average size of 30 μm between 15 μm and 45 μm. The metamaterial specimen consisted of BCCZ unit cells (derivative of BCC) as basic unit cells, consisting of four equilateral triangles with 12 rectangular struts. BCCZ lattice structure is characterized by simple topology, strong designability, strong manufacturability, and excellent mechanical properties [32]. Moreover, it is worth noting that the success rate of BCCZ lattice structure in AM is very high in millimeter scale manufacturing, which is mainly due to the tilt angle of the pillar in the BCCZ lattice structure [33]. The size of this unit cell is 4 mm, and the nominal thickness is 0.5 mm in both directions. The overall size of the structures is 80×32×32mm (composed of 8×8×20 cells). Figures 1 (a) and (b) show the schematic metamaterial design with unit cell dimensions. The xz-plane consists of 8-unit cells in both directions and 20-unit cells along the y-axis. Using the heat-treatment strategy, we heat-treated the specimens to improve the material properties (see Table 2 [31]). Figure 1 (c) shows the three as-built samples of metamaterials with a building plate, the built direction (vertical direction) of the samples were taken along the z-axis. The build plate was removed via wire cutting, maintaining the strut thickness of 0.5 mm. The relative density ρ of the BCCZ unit cell truss lattice material is given by:

$$\rho = \left(1 + \sqrt{3}\right)\left(\frac{2t}{l}\right)^2 \quad (1)$$

where t is the strut thickness in both direction and l is the unit cell length. The strength of a stretch dominated lattice structure with 10% relative density is three times stronger than an equivalent bending dominated foam [13,34]. Thus, the relative density value was taken as 0.13 for our investigation, considering the manufacturability of the minimum strut diameter [35].

Table 1. Chemical composition of the main elements in Inconel 718 powder (wt%) [31]

Elements in weight percent (wt%)									
Ni	Cr	Fe	Nb	Mo	Ti	Al	Co	Mg	Si
50 - 55	17 - 21	remainder	4.8 - 5.5	2.8 - 3.3	0.7 - 1.2	0.2 - 0.8	≤1.0	≤0.35	≤0.35

Table 2. Heat treatment procedures for cast Inconel 718 components [31]

Homogenization	Heat to 1093 °C±14, hold for 1 - 2 h, air cool or faster

Solution	Heat to 954 - 982 °C, hold for >1 h, air cool or faster
Ageing	Heat to 718 °C±8, hold for 8 h, furnace cool to 620 °C±8 in 1 h, hold for 10 h, air cool or faster

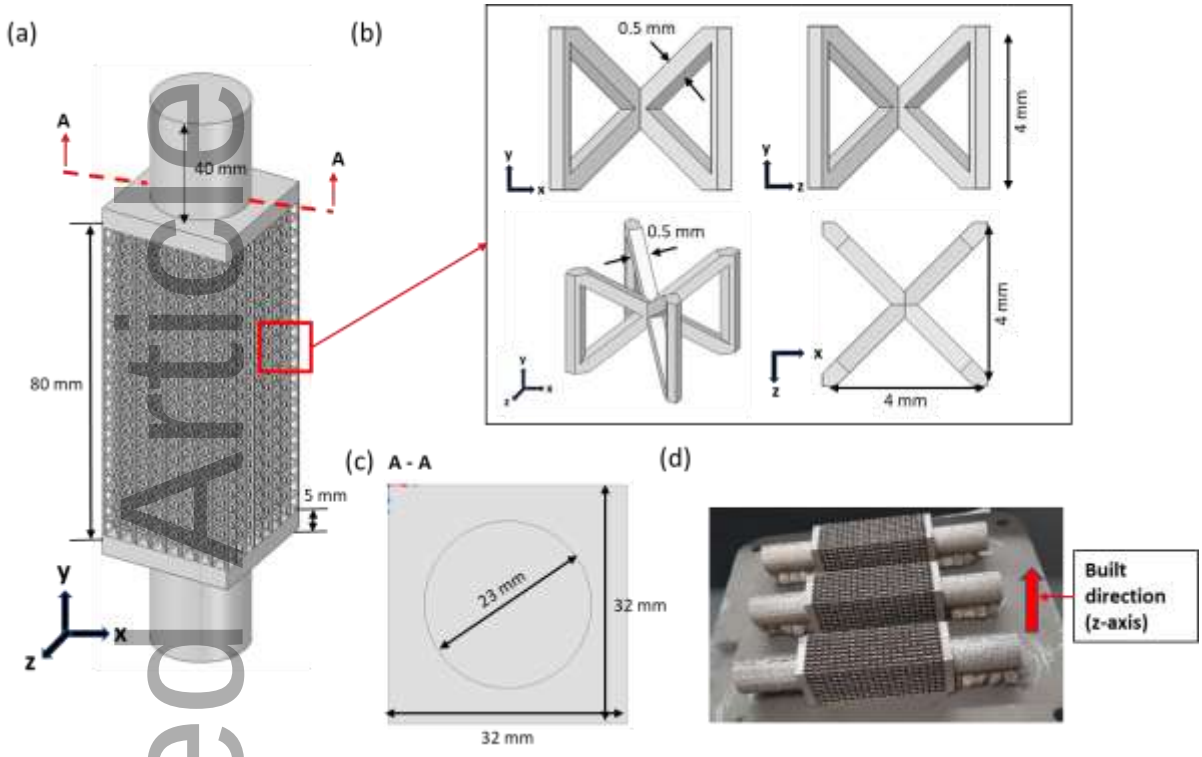

Figure 1 (a) CAD geometry of a BCCZ metamaterial with dimensions, (b) unit cell dimension of a BCCZ cell, (c) specimen clamp geometry dimensions, and (d) as-built specimens showing built direction with building plate.

2.2 Experimental study

2.2.1 Uniaxial tensile test at elevated temperature (650 °C)

It is essential to identify the yield strength of the metamaterials since any stress applied higher than the yield stress can lead to plastic deformation, leading to failure before the creep fracture has fully developed [36]. Hence, the yield strength, tensile strength and elongation of the bulk and lattice structure specimens during tension were evaluated by uniaxial tensile testing at 650 °C temperature and a constant strain rate of 0.02mm/sec on the Mayes ESM250 testing rig. The temperature 650 °C was identified due to inherent qualities of the Inconel 718 superalloy to retain high strength and fatigue resistance at elevated temperatures as high as 650 °C, which make this material one of the most popular materials applied in modern aero engines. The rig was fitted with a Mayes 250 kN load cell on the crosshead (a horizontal bar across the top part of the rig), which was used to measure the force during the test. The load cell also had the capability of measuring displacement in the region of the crosshead. A Mayes 240V split section resistance furnace was used to maintain the required temperature. The furnace body is split into two halves and hinged to accommodate easy sample insertion. The temperature in the furnace, along the gauge length of the specimen, was measured using three K-type thermocouples spaced out along the surface of the specimen. Two thermocouples were placed at

the top and bottom edges of the gauge length, and a third one was in the middle. The furnace had three independent heating elements, and each of them was connected to a thermocouple. The data from the thermocouples were used to adjust the temperature within the furnace, and the samples were equilibrated at the test temperature for 30 min before testing. The testing equipment was located in a room with a controlled air temperature of around 20 °C. The ends of the sample under testing were positioned in the designated holders with threads. The displacement was measured close to the boundaries of the gauge length. The displacement along the gauge length of the sample was measured using a pair of high-temperature side-contact linear voltage differential transformer (LVDT-0582) extensometers. The several key components of the Mayes ESM250 testing rig are shown in Figures 2 (a) and (b).

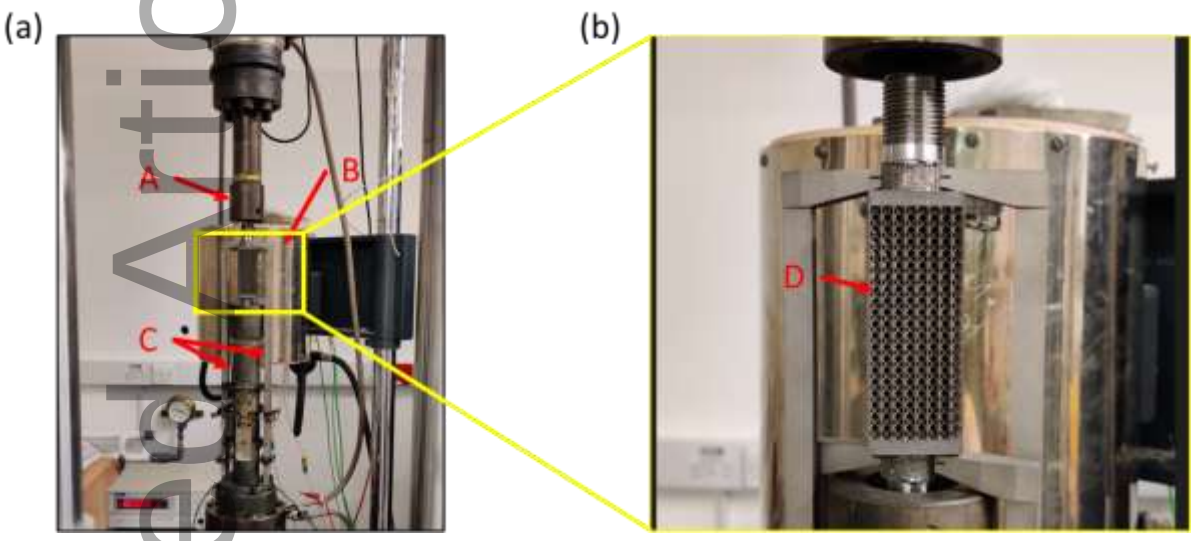

Figure 2 Testing rig based on the Mayes ESM250 electromechanical testing machine, used to conduct experimental tensile tests, consisting of; (a) "A" crosshead with a load cell, "B" split section thermal furnace with three independent heating elements, "C" a pair of linear voltage differential transformer extensometers (b) Zoom of the area consisting of metamaterial specimen "D".

2.2.2 Creep rupture tests

Creep tests were also carried out on the Mayes ESM250 testing rig. As mentioned in the above section, to reduce the influence of non-creep induced plastic deformation, uniaxial tension creep experiments were performed at the initially applied load levels of 35% and 70% of yield strength of metamaterials obtained via a tensile test in the air at 650 °C. The sample temperature was controlled by employing three thermocouples at the top, centre, and bottom of the specimen gauge length to ±0.5 °C of the set point. Creep strain measurements were obtained using an LVDT extensometer attached to the end sections of the specimen gauge length.

2.2.3 Microstructure characterisation

The microstructure of the Inconel 718 under creep tests was characterised by SEM equipped with an X-ray analysis system and 80 mm^2 silicon drift detector (SDD). Fractographic inspections were implemented on the fracture surface of the lattice specimens. Ruptured surfaces were sectioned from these specimens using electrical discharge machining (EDM), cleaned in an ultrasonic bath, and mounted on SEM stubs for imaging.

A JEOL 7000F field-emission SEM was employed to characterise fracture surfaces at a working distance of 15mm and an accelerating voltage of 15kV. Energy-dispersive X-ray spectroscopy (EDS) analysis was conducted using the Oxford Aztec software to confirm the nature of fractures. The working distance for EDS analysis was 11.5mm, and the accelerating voltage was 20kV.

2.3. Numerical modelling

2.3.1 The Finite element model

To identify the yield strength of the metamaterial, a tensile test at elevated temperature has been performed, and a numerical model has been deployed for numerical validation. The numerical model was established using finite element software ABAQUS/EXPLICIT. Timoshenko beam elements with linear interpolation functions (element type B31 in ABAQUS) were adopted to improve computational efficiency and ensure the accuracy of the simulations [37]. Numerical tests have suggested that converged results can be achieved with each strut meshed with 10 beam elements of equal length. All nodes on the bottom side of the lattice structure were constrained in translation and rotation degrees of freedom. All translational and rotation degrees of freedom were restricted for the upper surfaces of the structures except for the loading direction, as shown in Figure 3. Displacement control and smooth analysis were imposed to ensure the simulation was a quasi-static process. The quasi-static process was verified by maintaining the kinetic energy of the system at less than 5% of its internal energy [38].

The above FE model has been also used for creep life simulations using ABAQUS/IMPLICIT solver. Similarly, all nodes on the bottom side of the lattice structure were constrained and all degrees of freedom were restricted for the upper surfaces of the structures except for the loading direction where a constant loading force was applied. In the creep numerical calculations, a small initial time (1e-8 seconds), was used for structural loading before creep starts.

2.3.2 Material model

The Ramberg-Osgood model was used to represent the true stress-strain relationship of the parent material, i.e., additively manufactured Inconel 718, as illustrated in Figure 3 [39]:

$$\bar{\varepsilon} = \frac{\bar{\sigma}}{\bar{E}} + \kappa\left(\frac{\bar{\sigma}}{\bar{\sigma}_y}\right)^{\eta} \tag{2}$$

where $\bar{E} = 202\,GPa$ and $\bar{\sigma}_y = 755\,MPa$ are Young's modulus and yield stress of the Inconel 718, respectively; $\kappa = 0.002$ is the yield offset, and η is the hardening exponent. Thus, this material model is suitable for capturing the mechanical behaviour of LBPF manufactured as-built uniaxial tensile specimen (Inconel 718) under a tensile test at 650 ˚C. Note that during tensile or creep testing the temperature of the sample is maintained at a constant value which has been discussed later. Hence the temperature is limited to 650 ˚C, for more generalized approach the temperature dependent stress-strain curves need to be defined.

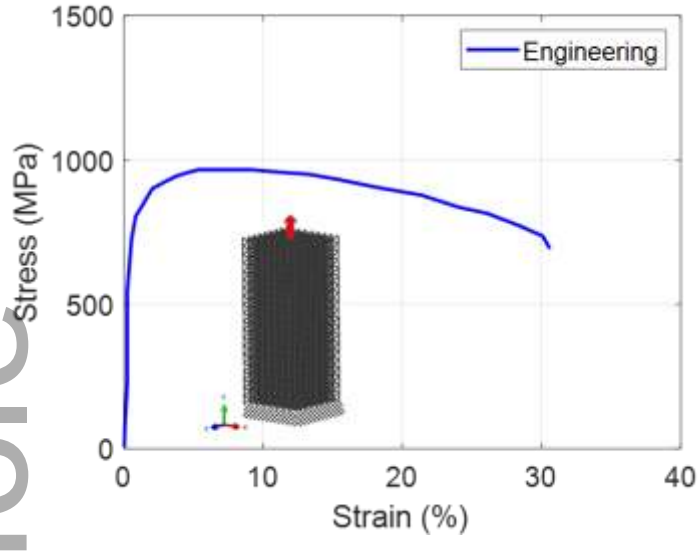

Figure 3 Engineering stress-strain curves of LBPF manufactured as-built uniaxial tensile specimen (Inconel 718) under tensile test at 650 ˚C, and an inserted figure of a typical FE model of the metamaterial.

Failure initiation starts when the maximum axial strain reaches 0.08 in the element based on the tensile test result in Figure 3. The strut necking behaviour was replicated by the reduction of the yield stress after failure initiates, which is characterised by the plastic damage variable *D*:

$$\bar{\sigma} = (1 - D)\bar{\sigma}_y \tag{3}$$

where *D* varies from 0 to 1, and is a function of the plastic strain, fitted to match the data of Figure 3. The corresponding element was deleted from the mesh when all the material points within the element failed (*D* = 1).

2.3.3 Kachanov's creep damage equations for the parent material

To understand the creep damage evolution in the parent material, including the tertiary stage of creep deformation, the creep damage model, initially proposed by Kachanov [40] and Rabotnov [41], is reasonably accurate in predicting the tertiary creep behaviour of the materials. Incorporating the damage state parameter ω, the creep strain rate is defined as follows:

$$\frac{d\varepsilon^c}{dt} = A\left(\frac{\sigma}{1-\omega}\right)^n t^m \tag{4}$$

where ε^c, σ and t are the creep strain, the uniaxial stress, and the time, respectively. The material constants *A* and *n* are the Norton law constants, which control secondary creep behaviour and can be determined from a log-log plot of the creep strain rate versus the applied stress [42], while the material constant *m* controls the primary creep strain. The creep damage parameter ω ranges from 0 to 1, corresponding to no damage state and complete failure of materials, respectively. The creep damage rate as a function of stress and current damage is described as

$$\frac{d\omega}{dt} = M\frac{(\sigma_r)^{\chi}}{(1+\phi)(1-\omega)^{\phi}}t^{m} \quad (5)$$

where, M, ϕ and χ are continuum damage material constants. ω is the damage parameter having a value in-between 0 (no damage) and 1 (100% damage/failure). The rupture stress σ_r is a dependent variable whose values change as per the maximum principal stress σ_1 and equivalent stress σ_{eq} as defined by the below equation:

$$\sigma_r = \alpha\sigma_1 + (1-\alpha)\sigma_{eq} \quad (6)$$

The above equation is suitable for mixed stress criteria of the material, where α is a material constant related to the tri-axial stress state of the material range from 0 to 1. The value of α determines the maximum principal stress dominant at 1 and equivalent stress dominant at 0, which is important for the multiaxial damage model. Although, the notched specimen uniaxial test needs to be performed to determine the value of α [43]. In our case, the value of α is zero since we have used the Timoshenko beam elements with linear interpolation functions (element type B31 in ABAQUS).

3. Determination of high-temperature properties at 650ºC

3.1 Tensile Strength

Figure 4 (a) compares the macroscopic stress-strain responses of the metamaterials subjected to uniaxial tension at 650 °C obtained via experiment and numerical calculation. The x-axis represents the applied macroscopic strain on the material, and the y-axis represents the corresponding macroscopic stress. The dashed curve represents the experimental results, and the continuous curve represents the results from the numerical simulation. It can be observed that both curves show very similar behaviors, which suggests that our numerical simulation could achieve high fidelity. The macroscopic stress-strain response has been used to identify two loading conditions for the creep test, i.e., 35% and 70% of yield strength (10 kN and 20 kN), as shown in Figure 4 (a). In Figure 4 (b) and (c), we have shown the strut damage parameter of numerical calculations and experimental results at fracture, respectively.

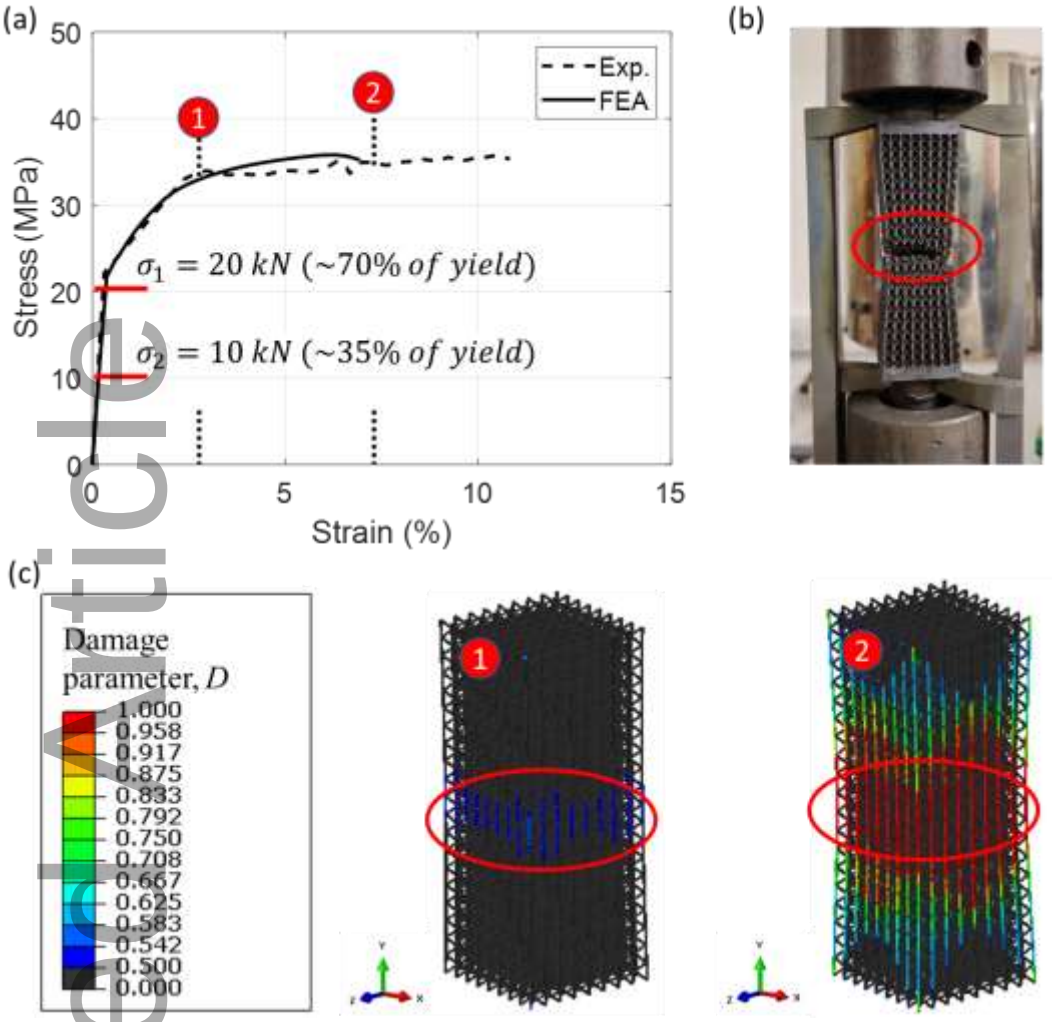

Figure 4 (a) A comparison between stress-strain curves obtained via experiment and FEA of a lattice specimen at 650°C. (b and c) the strut damage parameter of experimental and the numerical calculation results after the final fracture, respectively.

3.2 Creep properties and damage parameters estimation

In this section, we have used Kachanov's creep damage equation to calculate damage parameters. For relatively simple single state variables, Kachanov's equations, Equations. (4) and (5), the material constants A, n, m, M, ϕ and χ can be determined directly by fitting the uniaxial strain-time equation to a few uniaxial strain-time curves obtained from creep tests at a given temperature.

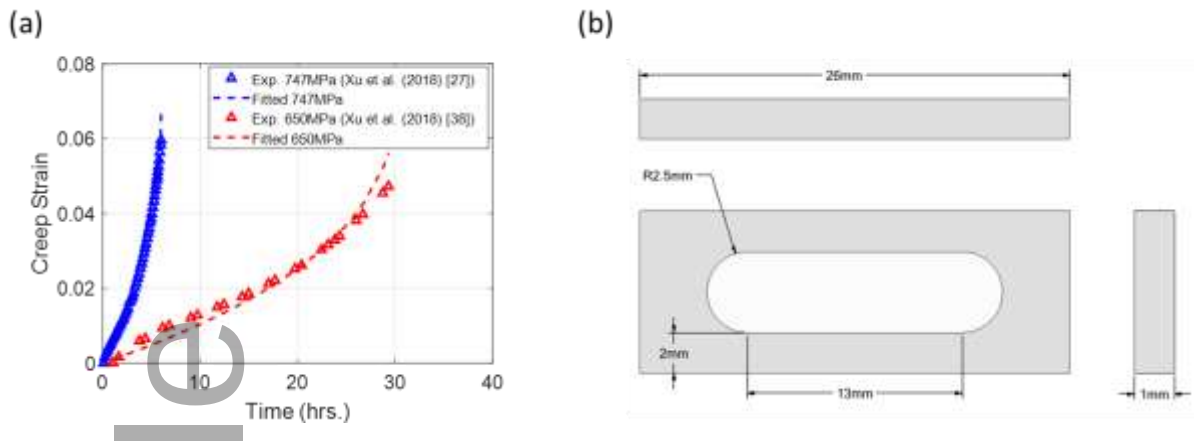

Figure 5 (a) Fitted and tested uniaxial creep strain curves of the parent material (b) dimensions of the two bar specimen (TBS) [44,45].

Figure 5 (a) shows the correlation between experimental and analytical data estimated through curve fitting at 650 MPa and 747 MPa stresses. The experimental creep curves have been reported by Xu et al. [36] at 650 MPa and Xu et al. [31] at 747 MPa stress conditions for Inconel 718 at an elevated temperature of 650 °C. The estimated damage parameters obtained from the literature after curve fitting are given in Table 3. The damage parameters given in Table 3 are based on the Two-bar specimens (TBS) [31,36,44,45], dimensions shown in Figure 5 (b). In their work, the TBS specimen surfaces were grounded and polished before testing to remove the milling-affected zone containing machining defects. However, due to the complexity of the metamaterial used in this work, the lattice strut surfaces have been experimented on as-built conditions. In addition, owing to manufacturing defects consisting of microstructure defects and size effects, the damage parameters were corrected for the creep material modelling. The inverse method mentioned by Wen et al. [46] was used for correction of the damage parameters. The updated damage parameters after the correction have also been provided in Table 3. The microstructures at the fracture surfaces of the metamaterial specimens have been discussed in the results section of this paper.

Table 3 Creep damage material constants (stress in MPa and time in hours) from literature and after correction

Creep Damage Constants	Inconel 718 at 650 ºC (from literature)	Inconel 718 at 650 ºC (after correction)
A	3.54×10^{-35}	4.54×10^{-35}
n	11.167	11.9
m	0	0
M	5.13×10^{-35}	4.44×10^{-33}
∅	15.25	12.0
χ	11.662	5.416
α	0.0	0.0

4. Results and discussion

4.1 Creep behaviour

Figures 6 (a) and (b) show the correlation between experimental and numerical simulation results under 20 kN and 10 kN loads, respectively. For 10 kN loading condition, the numerical result has accurately captured the creep behaviour, whereas for 20 kN the numerical result is reasonably close to experimental result of metamaterials at 650 °C. Furthermore, at the 20 kN load, the metamaterial fails very early owing to brittle fracture compared to the 10 kN loading. The differences in the creep life of metamaterials show that the failure mechanisms have been significantly affected by loading conditions. Figures 7 (a) and 8 (a) show the progression of the equivalent stresses illustrating stress relaxation at different life fractions for a typical unit cell at 20 kN and 10 kN loads, respectively. The representative unit cell has been taken considering maximum creep damage, ω, occurring (indicated by a black circle) in the middle of the metamaterial specimen, as shown in Figure 9 (a). Similarly, Figures 7 (b) and 8 (b) show the creep strains and Figures 7 (c) and 8 (c) show the creep damage, ω, evolution of the unit cell. The FE results show that the creep strain and creep damage progression at 20 kN load are significantly higher than 10 kN load for their corresponding time creep life ratio. For example, at 20 kN load and $t/t_f = 0.64$ the creep damage is ~0.25 and at 10 kN load and $t/t_f = 0.52$ the creep damage is ~0.08 (Figures 7 (c) and 8 (c)). At 20 kN load, the struts have higher stresses than the yield stress of the parent material (see Figure 9 (b)), leading to higher plastic strain and plastic damage. The metamaterial failed at a very early stage at 20 kN load due to plasticity damage rather than creep damage. However, at 10 kN load, the struts have lower stresses than 20 kN load, leading to failure due to primarily creep fracture. Figures 9 (c) and (d) show the creep strain and creep damage evolution of the strut experiencing maximum creep damage in the metamaterial specimen. The creep strain at failure for both loading conditions are reasonably close to 0.12, however at 20 kN load the failure time is $t_f = 78$ seconds and for 10 kN load the failure time is $t_f = 123$ hours. This indicates that the creep strain rate is much higher at 20 kN compared to the

10 kN load. Similarly, the creep damage rate at 20 kN load is significantly higher compared to 10 kN load and failure occurs when creep damage value reaches at 1.

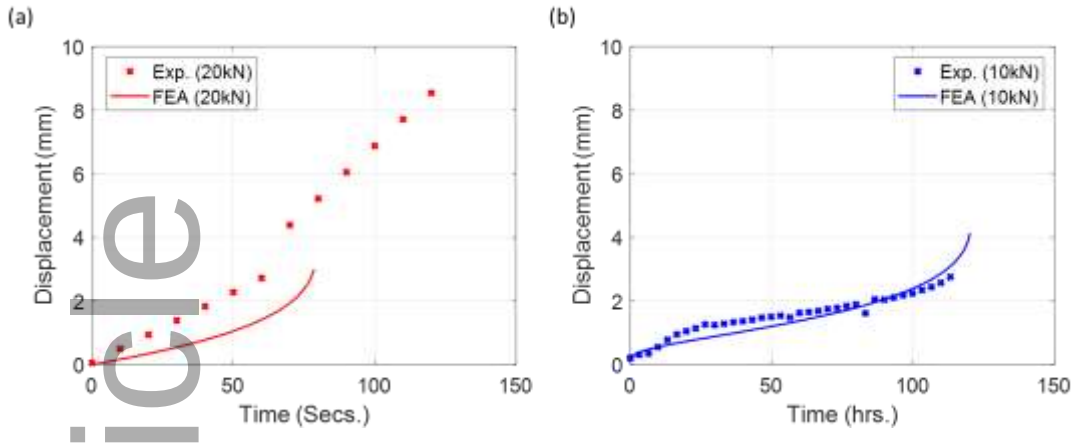

Figure 6 creep curves showing the correlation between experimental versus FEA results of metamaterials samples under (a) 20 kN and (b) 10 kN loads at 650 °C

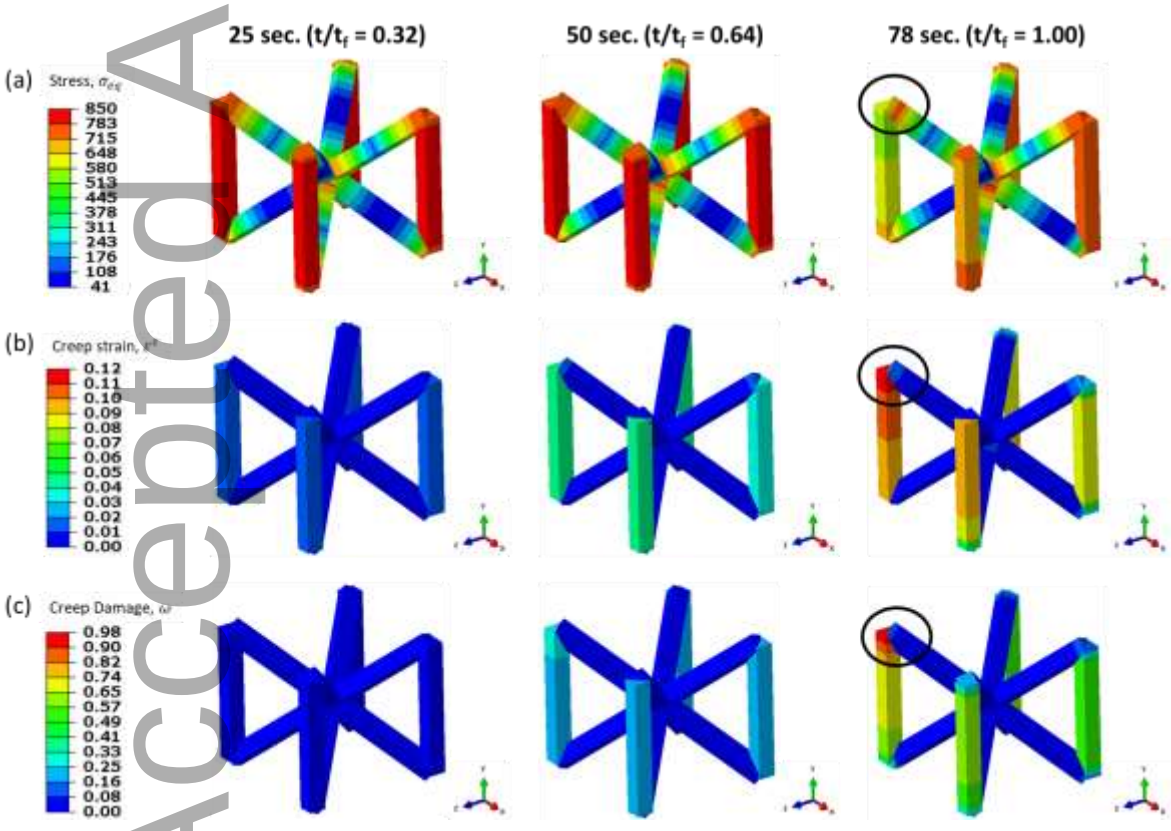

Figure 7 Creep behaviour of the metamaterials showing the progression of (a) equivalent stresses (b) creep strains and (c) creep damage at different times at 20 kN load.

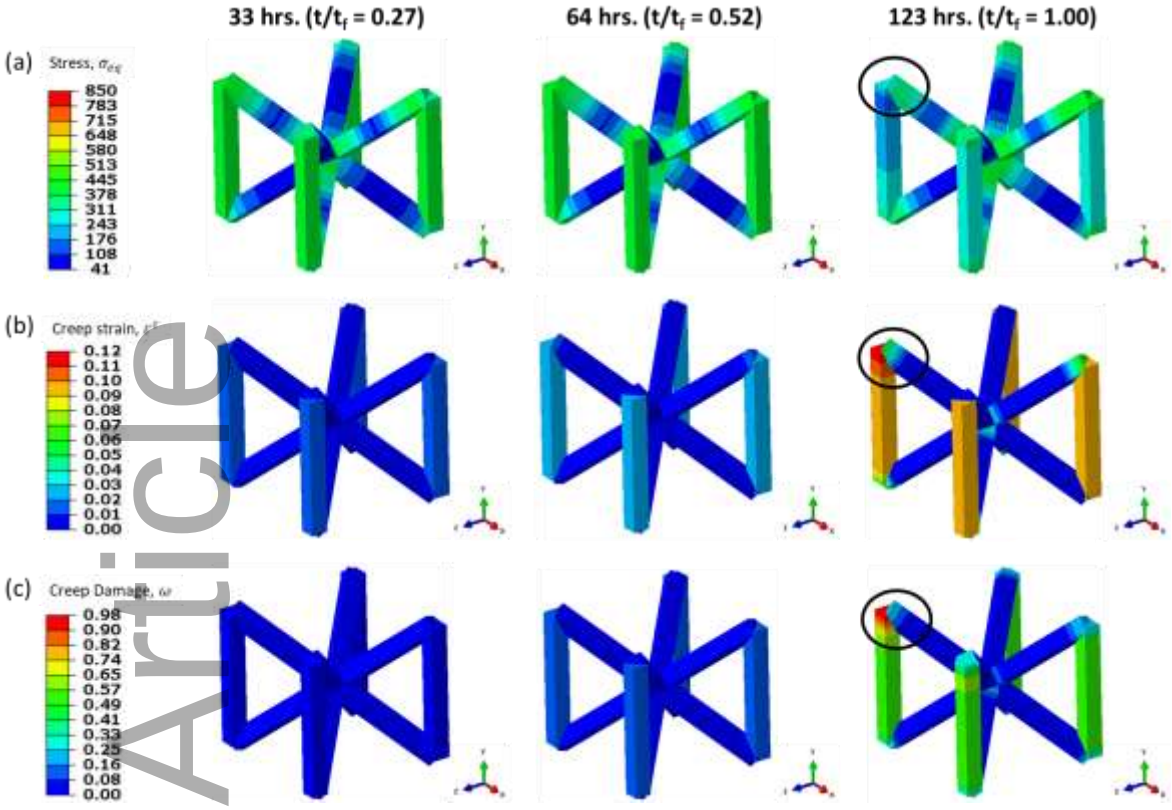

Figure 8 Creep behaviour of the metamaterials showing the progression of (a) equivalent stresses (b) creep strains and (c) creep damage at different times at 10 kN load.

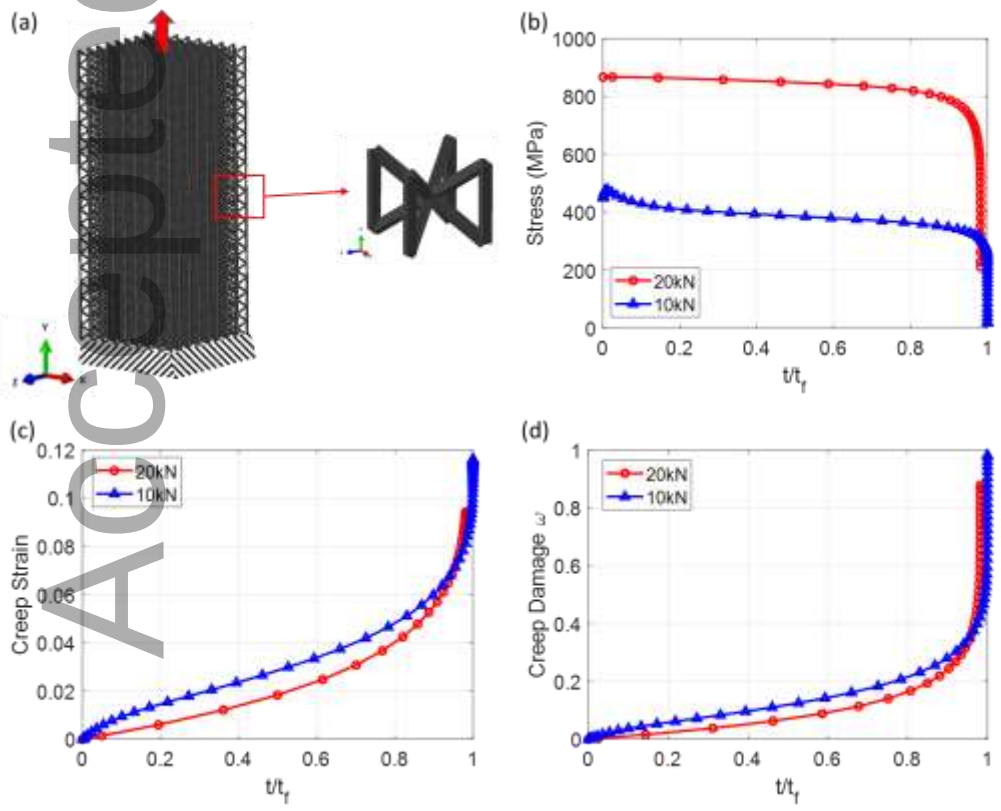

Figure 9 (a) the position of a typical unit cell in the big lattice specimen, (b) the stress, (c) the creep strain, and (d) creep damage, ω, evolution (till failure) at the maximum creep damage area for both 10 kN and 20 kN loads

4.2 Microstructures and fractography

To confirm the 3D printing quality, a representative specimen before the creep tests has been selected for SEM imaging. Figure 10 (a) shows the microstructure at the truss joint, and Figure 10 (b) shows an overall view of a typical BCCZ unit cell. Although some metal particles were observed sticking to the BCCZ lattice due to insufficient melting, no significant manufacturing defects were observed at the BCCZ structure before the creep tests. The microstructures at the truss joint and surface exhibit a smooth texture, shown in Figures 10 (a) and (b), respectively.

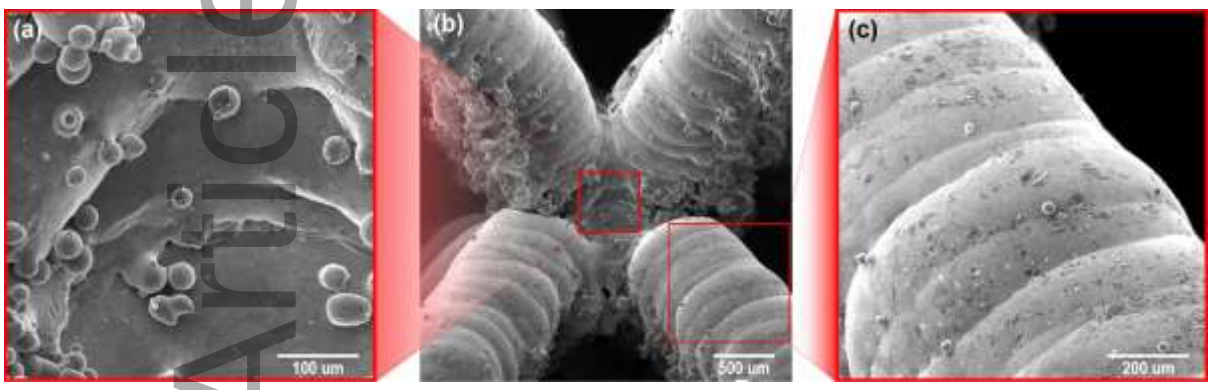

Figure 10 (a) Microstructure at the truss joint. (b) An overall view of a typical BCCZ unit cell. and (c) Microstructure at the surface of the BCCZ truss.

Figure 11 (a) shows the overview of the fracture surface for metamaterial samples under a 10 kN load. The onset of crack was observed at the edge of the specimens, which propagated transversely. To investigate the nature of failure, the fracture surface where the crack initials were examined using SEM. The fracture surface of metamaterials samples under 10 kN load exhibits a co-existence of brittle and ductile features in the vicinity of a 400μm microcrack, as shown in Figures 11 (c) to (f). Figures 11 (c) and (d) show the regions of transgranular cleavage and quasi-cleavage with typical feather markings and river patterns, which indicates a feature of brittle fracture. In contrast, Figure 11 (f) shows typical ductile failure with a certain amount of inclusions embedded into deep dimples. The appearances of transgranular and quasi-cleavage indicate a region of higher hardness, which was similar to those reported by Martin et al. [47] and Lynch [48], may attribute to the coalescence or growth of micro-voids that initiate within intense slip band intersections. The presence of inclusions and deep dimples indicates a lower hardness in the region of ductile fracture, which may cause local softening under the tensile load. A variation of hardness in the vicinity of the microcrack may result in stress heterogeneity that facilitates the formation or propagation of micro-voids under creep load and eventually forms a microcrack causing structural failure.

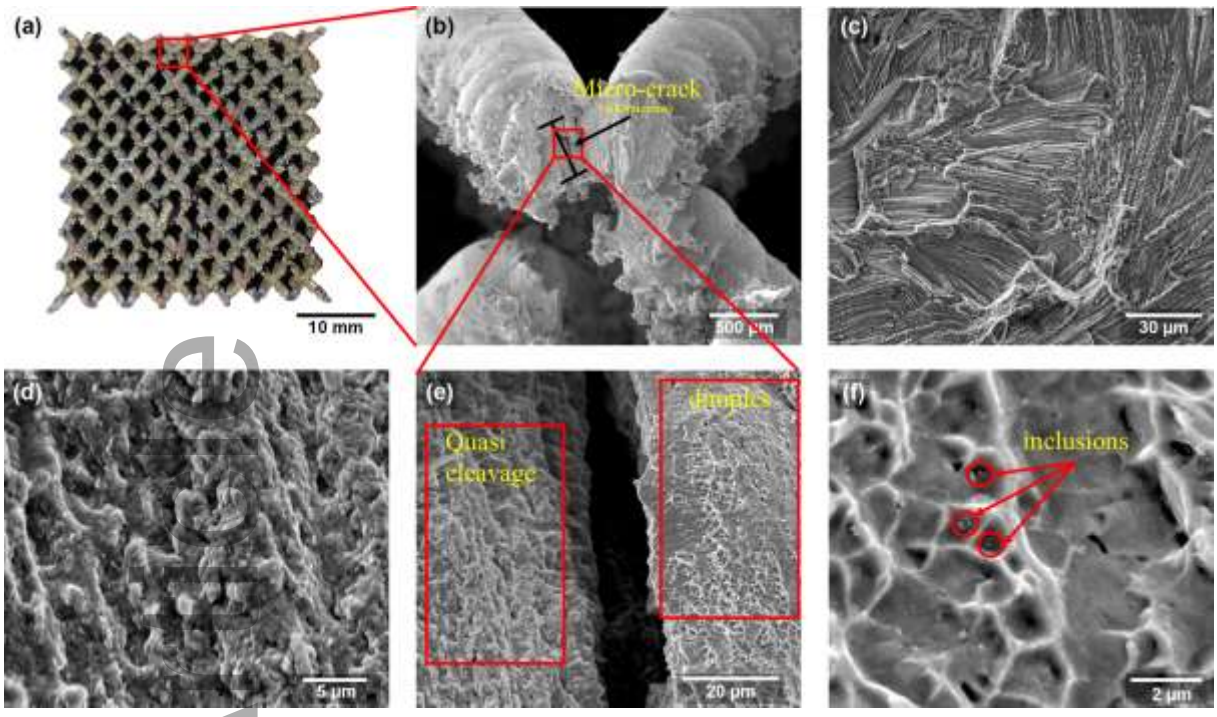

Figure 11 (a) An overview of the fracture surface for the specimen failure under 10kN load. (b) The fracture surface of the crack initiates. (c) Fracture features at the region of transgranular cleavage. (d) Fracture features at quasi-cleavage surface. (e) Co-existence of brittle and ductile features in the vicinity of the microcrack. (f) Deep dimples with inclusions near the microcrack.

Figure 12 (a) shows the overview of the fracture surface for the metamaterial sample under a 20 kN load. The SEM images of the fracture surface where the crack initiates exhibit a typical brittle failure, as shown in Figures 12 (b) and (c). Unlike the sample that failed under a 10 kN load, a clear transgranular cleavage without any inclusions was observed across the whole fracture surface. A region with dull spots shows an alternating light, and a dark feature was found at the edge of the cross-section of the lattice truss, as shown in Figure 12 (c). EDS analysis was implemented to further confirm the composition of the element at dull spots. The x-ray emission spectrum (Figure 12 (d)) and EDS elemental mapping (Figure 12 (e)) indicate that the alloying elements were a mixture of oxygen, chromium, carbon, nickel, iron, and calcium. Notably, a high carbon content region was also found in the EDS elemental mapping, as shown in Figure 12 (e). Although there is a limited basis in literature to claim that carbides may directly lead to an earlier failure, the presence of carbides cannot be considered as benign in additive manufacturing as it can increase the local hardness and behave as a source of crack nucleation that reduces the local strength and toughness.

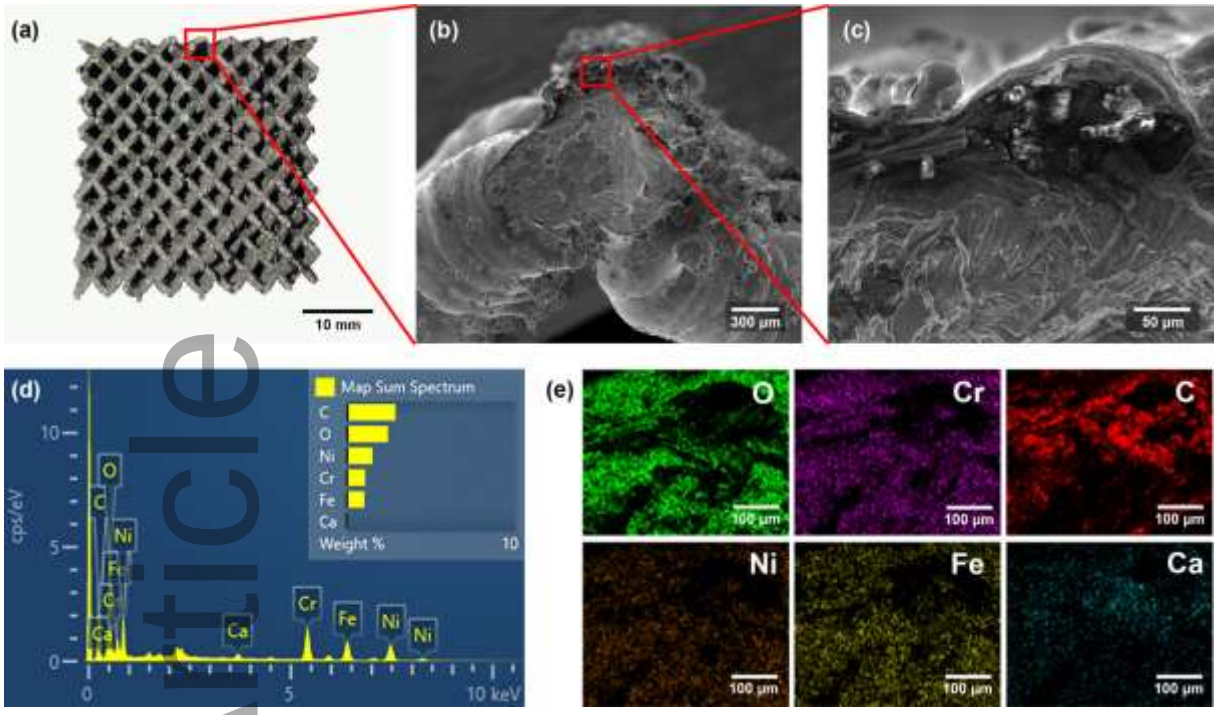

Figure 12 (a) An overview of the fracture surface for specimen failure under 20kN load. (b) The fracture surface of the crack initiates. (c) EDS mapping area of the dull spots region. (d) and (e) X-ray emission spectrum and EDS elemental mapping at the dull spots region, respectively.

4.3 Creep performance of metamaterials

Here, we have shown the creep performance of the metamaterials at different loadings and relative densities obtained via numerical calculations. The x-axis shows the loading conditions and relative densities in Figures 13 (a) and (b), respectively, and the creep life has been plotted on the y-axis on a logarithmic scale. Figure 13 (a) shows the impact of loading conditions on the creep life of metamaterials. It shows that the experimental data and FE results correlate reasonably, and Figure 13 (b) shows the increase in creep life with respect to relative density obtained via FE calculations. Relative densities of the metamaterial designs were obtained by adjusting the strut thickness, t and maintaining other parameters constant in the numerical model. It can be observed that the creep life decreases significantly with the loading, and the creep life increases with the relative density. Additionally, the impact of the relative density of the metamaterials is significant on creep failure life, subjected to different loading conditions.

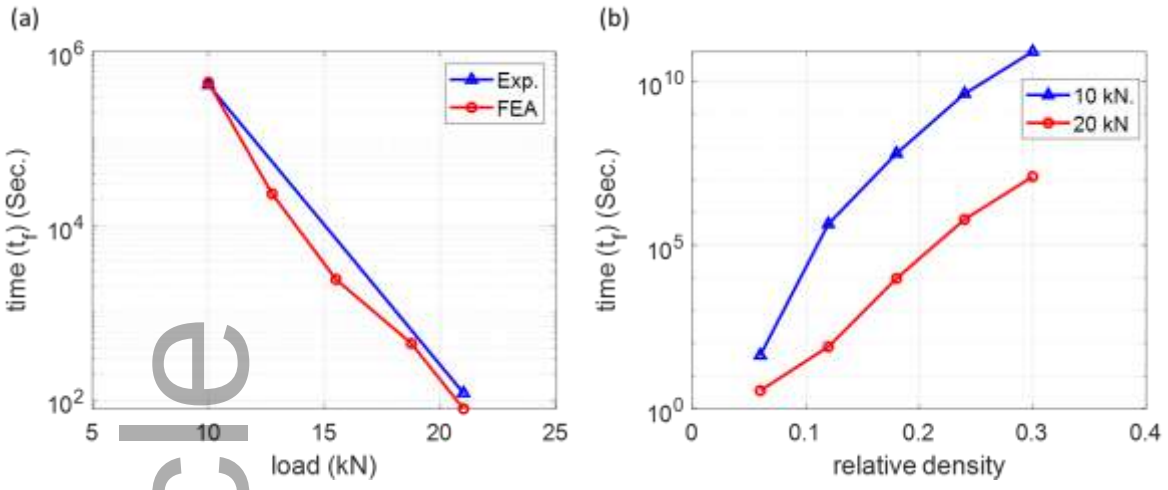

Figure 13 (a) the impact of loading conditions on the creep life of metamaterials comparison between test data and FE data (b) the increase in creep life with respect to relative density obtained via FE calculations.

5. Conclusion

This study investigated the creep behaviour of lattice metamaterials manufactured by LPBF using Inconel 718 at an elevated temperature of 650°C. The microstructural defects, such as suboptimal grain size and morphology, and macroscale anomalies, such as lack of fusion, present in LPBF materials led to performance degradation for creep mechanical properties. Through the use of microstructural characterisation and Kachanov's damage modelling, it has been found that the creep performance of the metamaterials was affected by the microstructure defects. We have shown that, due to the LPBF, which can result in the presence of inclusions, microcracks, and deep dimples, local softening may occur under tensile load leading to an earlier failure compared to conventional manufacturing processes. Furthermore, the numerical calculations and experiment results showed a logarithmic decay in creep life with increased applied load. This is caused by high stress induced on the struts of the metamaterials, which leads to early failure owing to plastic deformation. The numerical calculations also shows that the creep life increases with increase in relative density. Note that Kachanov's model does not consider plasticity damage, and viscoplastic model is recommended for higher loading.

These findings provide a deeper understanding of the creep behaviour of LPBF metamaterials and can inform the optimisation of LPBF manufacturing processes to improve the mechanical properties of metamaterials. However, the paper does not address important topics, such as the impact of strut size effects, LPBF building direction and residual stress on creep testing. Therefore, it is recommended for future study that to represent the size effect; ideally, miniaturised tensile and creep tests (~0.5mm specimen, i.e., size of the strut) at 650°C should be carried out to derive the material properties, for lattice modelling. Additionally, future work needs to be conducted by undertaking more creep testing and modelling with different parameters such as loads, temperatures, and lattice types to allow a better understanding of the creep behaviour of metamaterials.

References

1. Boyer RR. 1996. An overview on the use of titanium in the aerospace industry. *Mater Sci Eng A*. (doi:10.1016/0921-5093(96)10233-1)

2. Kuziak R, Kawalla R, Waengler S. 2008. Advanced high strength steels for automotive industry: A review. Archives of Civil and Mechanical Engineering. 2008. (doi:10.1016/s1644-9665(12)60197-6)

3. Xue Z, Hutchinson JW. 2004. A comparative study of impulse-resistant metal sandwich plates. *Int J Impact Eng*. (doi:10.1016/j.ijimpeng.2003.08.007)

4. Kim T, Hodson HP, Lu TJ. 2004. Fluid-flow and endwall heat-transfer characteristics of an ultralight lattice-frame material. *Int J Heat Mass Transf*. (doi:10.1016/j.ijheatmasstransfer.2003.10.012)

5. Wang J, Lu TJ, Woodhouse J, Langley RS, Evans J. 2005. Sound transmission through lightweight double-leaf partitions: Theoretical modelling. *J Sound Vib*. (doi:10.1016/j.jsv.2004.10.020)

6. Liu T, Deng ZC, Lu TJ. 2007. Bi-functional optimization of actively cooled, pressurized hollow sandwich cylinders with prismatic cores. *J Mech Phys Solids*. (doi:10.1016/j.jmps.2007.04.007)

7. Yang W, Yue Z, Xu B. 2016. A hybrid elastomeric foam-core/solid-shell spherical structure for enhanced energy absorption performance. *Int J Solids Struct*. (doi:10.1016/j.ijsolstr.2016.05.001)

8. Yang W, Liu Q, Gao Z, Yue Z, Xu B. 2018. Theoretical search for heterogeneously architected 2D structures. *Proc Natl Acad Sci U S A*. (doi:10.1073/pnas.1806769115)

9. Bhuwal AS, Liu T, Ashcroft I, Sun W. 2021. Localization and coalescence of imperfect planar FCC truss lattice metamaterials under multiaxial loadings. *Mech Mater*. **160**:103996. (doi:10.1016/j.mechmat.2021.103996)

10. Tancogne-Dejean T, Mohr D. 2018. Elastically-isotropic elementary cubic lattices composed of tailored hollow beams. *Extrem Mech Lett*. (doi:10.1016/j.eml.2018.04.005)

11. Bonatti C, Mohr D. 2017. Large deformation response of additively-manufactured FCC metamaterials: From octet truss lattices towards continuous shell mesostructures. *Int J Plast*. (doi:10.1016/j.ijplas.2017.02.003)

12. Santorinaios M, Brooks W, Sutcliffe CJ, Mines RAW. 2006. Crush behaviour of open cellular lattice structures manufactured using selective laser melting. In: WIT Transactions on the Built Environment. 2006. (doi:10.2495/HPSM06047)

13. Gibson I, Rosen DW, Stucker B. 2010. Additive manufacturing technologies: Rapid prototyping to direct digital manufacturing. Additive Manufacturing Technologies: Rapid Prototyping to Direct Digital Manufacturing. 2010. (doi:10.1007/978-1-4419-1120-9)

14. Sing SL, Wiria FE, Yeong WY. 2018. Selective laser melting of lattice structures: A statistical approach to manufacturability and mechanical behavior. *Robot Comput Integr Manuf*. (doi:10.1016/j.rcim.2017.06.006)

15. Wang F. 2012. Mechanical property study on rapid additive layer manufacture Hastelloy® X alloy by selective laser melting technology. *Int J Adv Manuf Technol*. (doi:10.1007/s00170-011-3423-2)

16. Schafrik RE, Ward DD, Groh JR. 2001. Application of alloy 718 in GE aircraft engines: past, present and next five years. In: Proceedings of the International Symposium on Superalloys and Various Derivatives. 2001. (doi:10.7449/2001/superalloys_2001_1_11)

17. Diltemiz SF, Zhang S. 2016. Superalloys for super jobs. In: Aerospace Materials Handbook. 2016. (doi:10.1201/b13044-6)

18. Qi H, Azer M, Ritter A. 2009. Studies of standard heat treatment effects on microstructure and mechanical properties of laser net shape manufactured INCONEL 718. *Metall Mater Trans A Phys Metall Mater Sci*. (doi:10.1007/s11661-009-9949-3)

19. Liu F, Lin X, Yang G, Song M, Chen J, Huang W. 2011. Microstructure and residual stress of laser rapid formed Inconel 718 nickel-base superalloy. *Opt Laser Technol*. (doi:10.1016/j.optlastec.2010.06.015)

20. Amato KN, Gaytan SM, Murr LE, Martinez E, Shindo PW, Hernandez J, et al. 2012. Microstructures and mechanical behavior of Inconel 718 fabricated by selective laser melting. *Acta Mater*. (doi:10.1016/j.actamat.2011.12.032)

21. Thompson MK, Moroni G, Vaneker T, Fadel G, Campbell RI, Gibson I, et al. 2016. Design for Additive Manufacturing: Trends, opportunities, considerations, and constraints. *CIRP Ann - Manuf Technol*. (doi:10.1016/j.cirp.2016.05.004)

22. Bhuwal AS, Pang Y, Ashcroft I, Sun W, Liu T. 2023. Discovery of quasi-disordered truss metamaterials inspired by natural cellular materials. *J Mech Phys Solids*. (doi:10.1016/j.jmps.2023.105294)

23. Hu YN, Wu SC, Withers PJ, Zhang J, Bao HYX, Fu YN, et al. 2020. The effect of manufacturing defects on the fatigue life of selective laser melted Ti-6Al-4V structures. *Mater Des*. (doi:10.1016/j.matdes.2020.108708)

24. Peng X, Wu S, Qian W, Bao J, Hu Y, Zhan Z, et al. 2022. The potency of defects on fatigue of additively manufactured metals. *Int J Mech Sci*. (doi:10.1016/j.ijmecsci.2022.107185)

25. Song B, Zhao X, Li S, Han C, Wei Q, Wen S, et al. 2015. Differences in microstructure and properties between selective laser melting and traditional manufacturing for fabrication of metal parts: A review. Frontiers of Mechanical Engineering. 2015. (doi:10.1007/s11465-015-0341-2)

26. Mizokami Y, Igari T, Kawashima F, Sakakibara N, Tanihira M, Yuhara T, et al. 2013. Development of structural design procedure of plate-fin heat exchanger for HTGR. *Nucl Eng Des*. (doi:10.1016/j.nucengdes.2012.09.013)

27. Andrews EW, Gibson LJ, Ashby MF. 1999. Overview No. 132: The creep of cellular solids. *Acta Mater*. **47**(10):2853–63. (doi:10.1016/S1359-6454(99)00150-0)

28. Fan ZG, Chen CQ, Lu TJ. 2012. Multiaxial creep of low density open-cell foams. *Mater Sci Eng A*. (doi:10.1016/j.msea.2012.01.086)

29. Su B, Zhou Z, Wang Z, Li Z, Shu X. 2014. Effect of defects on creep behavior of cellular materials. *Mater Lett*. (doi:10.1016/j.matlet.2014.07.185)

30. MONKMAN F. C. 1956. An Empirical Relationship between Rupture Life and Minimum Creep Rate in Creep-Rupture Tests. *Proc ASTM*. **56**:593–620.

31. Xu Z, Hyde CJ, Tuck C, Clare AT. 2018. Creep behaviour of inconel 718 processed by laser powder bed fusion. *J Mater Process Technol*. (doi:10.1016/j.jmatprotec.2018.01.040)

32. Lei H, Li C, Meng J, Zhou H, Liu Y, Zhang X, et al. 2019. Evaluation of compressive properties of SLM-fabricated multi-layer lattice structures by experimental test and μ-CT-based finite element analysis. *Mater Des*. (doi:10.1016/j.matdes.2019.107685)

33. Li H, Yang W, Ma Q, Qian Z, Yang L. 2022. Specific Sensitivity Analysis and Imitative Full Stress Method for Optimal BCCZ Lattice Structure by Additive Manufacturing. *Crystals*. (doi:10.3390/cryst12121844)

34. Deshpande VS, Ashby MF, Fleck NA. 2001. Foam topology: Bending versus stretching dominated architectures. *Acta Mater*. (doi:10.1016/S1359-6454(00)00379-7)

35. Tankasala HC, Deshpande VS, Fleck NA. 2017. Tensile response of elastoplastic lattices at finite strain. *J Mech Phys Solids*. (doi:10.1016/j.jmps.2017.02.002)

36. Xu Z, Murray JW, Hyde CJ, Clare AT. 2018. Effect of post processing on the creep performance of laser powder bed fused Inconel 718. *Addit Manuf*. (doi:10.1016/j.addma.2018.10.027)

37. Fleck NA, Qiu XM. 2007. The damage tolerance of elastic-brittle, two-dimensional isotropic lattices. *J Mech Phys Solids*. (doi:10.1016/j.jmps.2006.08.004)

38. Geng X, Lu Y, Liu C, Li W, Yue Z. 2019. Fracture characteristic analysis of cellular lattice structures under tensile load. *Int J Solids Struct*. **163**:170–7. (doi:10.1016/j.ijsolstr.2019.01.006)

39. Firoz R, Basantia SK, Khutia N, Bar HN, Sivaprasad S, Murthy GVS. 2020. Effect of microstructural constituents on mechanical properties and fracture toughness of Inconel 718 with anomalous

deformation behavior at 650 °C. *J Alloys Compd*. (doi:10.1016/j.jallcom.2020.156276)

40. Kachanov LM. 1958. Time of rupture process under creep conditions. *Isv Akad Nauk SSR Otd Tekh Nauk*.

41. Rabotnov YN, Leckie FA, Prager W. 1970. Creep Problems in Structural Members. *J Appl Mech*. (doi:10.1115/1.3408479)

42. Hyde TH, Xia L, Becker AA. 1996. Prediction of creep failure in aeroengine materials under multi-axial stress states. *Int J Mech Sci*. (doi:10.1016/0020-7403(95)00063-1)

43. Hyde TH, Sun W, Williams JA. 1999. Prediction of creep failure life of internally pressurised thick walled CrMoV pipes. *Int J Press Vessel Pip*. (doi:10.1016/S0308-0161(99)00078-2)

44. Hyde TH, Ali BSM, Sun W. 2013. Analysis and design of a small, two-bar creep test specimen. *J Eng Mater Technol*. (doi:10.1115/1.4025192)

45. Ali BSM, Hyde TH, Sun W. 2016. Small Two-Bar Specimen Creep Testing of Grade P91 Steel at 650°C. *High Temp Mater Process*. (doi:10.1515/htmp-2014-0188)

46. Wen W, Sun W, Becker AA. 2019. A two-material miniature specimen test method and the associated inverse approach for high temperature applications. *Theor Appl Fract Mech*. (doi:10.1016/j.tafmec.2018.10.008)

47. Martin ML, Fenske JA, Liu GS, Sofronis P, Robertson IM. 2011. On the formation and nature of quasi-cleavage fracture surfaces in hydrogen embrittled steels. *Acta Mater*. (doi:10.1016/j.actamat.2010.11.024)

48. Lynch SP. 1984. A fractographic study of gaseous hydrogen embrittlement and liquid-metal embrittlement in a tempered-martensitic steel. *Acta Metall*. (doi:10.1016/0001-6160(84)90204-9)

Journal's Table of Contents (ToC)

This paper investigates the creep characteristics of additively manufactured Inconel 718 metamaterials. The creep behaviour of the metamaterials and the effects of microstructural defects is being assessed, and we have accurately captured the effects of the microstructure defects using Kachanov's creep damage model. In addition, the paper examines the leading causes of specimen failure and the effects of loading and relative density on creep life.